



Source Characterization and Tsunami Modeling of Submarine Landslides Along the Yucatán Shelf/Campeche Escarpment, Southern Gulf of Mexico

JASON D. CHAYTOR,¹ ERIC L. GEIST,² CHARLES K. PAULL,³ DAVID W. CARESS,³ ROBERTO GWIAZDA,³
JAIME URRUTIA FUCUGAUCHI,⁴ and MARIO REBOLLEDO VIEYRA⁵

Abstract—Submarine landslides occurring along the margins of the Gulf of Mexico (GOM) represent a low-likelihood, but potentially damaging source of tsunamis. New multibeam bathymetry coverage reveals that mass wasting is pervasive along the Yucatán Shelf edge with several large composite landslides possibly removing as much as 70 km³ of the Cenozoic sedimentary section in a single event. Using GIS-based analysis, the dimensions of six landslides from the central and northern sections of the Yucatán Shelf/Campeche Escarpment were determined and used as input for preliminary tsunami generation and propagation models. Tsunami modeling is performed to compare the propagation characteristics and distribution of maximum amplitudes throughout the GOM among the different landslide scenarios. Various factors such as landslide geometry, location along the Yucatán Shelf/Campeche Escarpment, and refraction during propagation result in significant variations in the affected part of the Mexican and US Gulf Coasts. In all cases, however, tsunami amplitudes are greatest along the northern Yucatán Peninsula.

1. Introduction

The Yucatán Shelf (Fig. 1) is the submerged portion of a broad carbonate platform that has been the site of carbonate deposition and removal since the Mesozoic. The steep and heavily eroded Campeche Escarpment marks the northern margin of the platform. Until high-resolution bathymetry data was collected in 2013 (Paull et al. 2014), the Yucatán Shelf

edge and Campeche Escarpment comprised the last remaining large area of the Gulf of Mexico (GOM) not evaluated for landslide-generated tsunami hazards (Chaytor et al. 2010; Horrillo et al. 2010). Although submarine landslide-generated tsunamis are low-likelihood events, they are one of the primary tsunami hazards in areas where the influence of active tectonic is low to absent. Compiled tsunami observation records for the GOM contains only one non-earthquake generated tsunami event (1922 Galveston) that may have been generated by a local submarine landslide [National Geophysical Data Center/World Data Service (NGDC/WDS)]. Paleotsunami deposits have been reported from locations along the GOM coasts, primarily thought to originate from tsunamis generated by the Chicxulub impact event (Bourgeois et al. 1988; Lawton et al. 2005), although some of these interpretations have been questioned (Adatte et al. 1996). Shaw and Benson (2015) report the occurrence of possible paleotsunami deposits along the Caribbean coast of Yucatán coast, but couldn't conclusively rule out a hurricane-generated origin. Nevertheless, submarine landslide generated tsunamis, constitute a significant hazard to coastal populations and critical infrastructure, but are often poorly constrained due to limited data on potential source characteristics.

Little is known about the origins and stratigraphy of the Yucatán Shelf located north of the Yucatán Peninsula, but the work of Bryant et al. (1969), Lindsay et al. (1975), Locker and Buffler (1983) and others found the nearly flat lying Cretaceous carbonate strata overlain by Cenozoic sediments to be generally analogous to the more studied West Florida Shelf situated along the eastern margin of the GOM. Complexities identified in comparisons of the

¹ U.S. Geological Survey, Woods Hole, MA, USA. E-mail: jchaytor@usgs.gov

² U.S. Geological Survey, Menlo Park, CA, USA.

³ Monterey Bay Aquarium Research Institute, Moss Landing, CA, USA.

⁴ Universidad Nacional Autónoma de México, Mexico City, Mexico.

⁵ Centro de Investigación Científica de Yucatán, Mérida, Mexico.

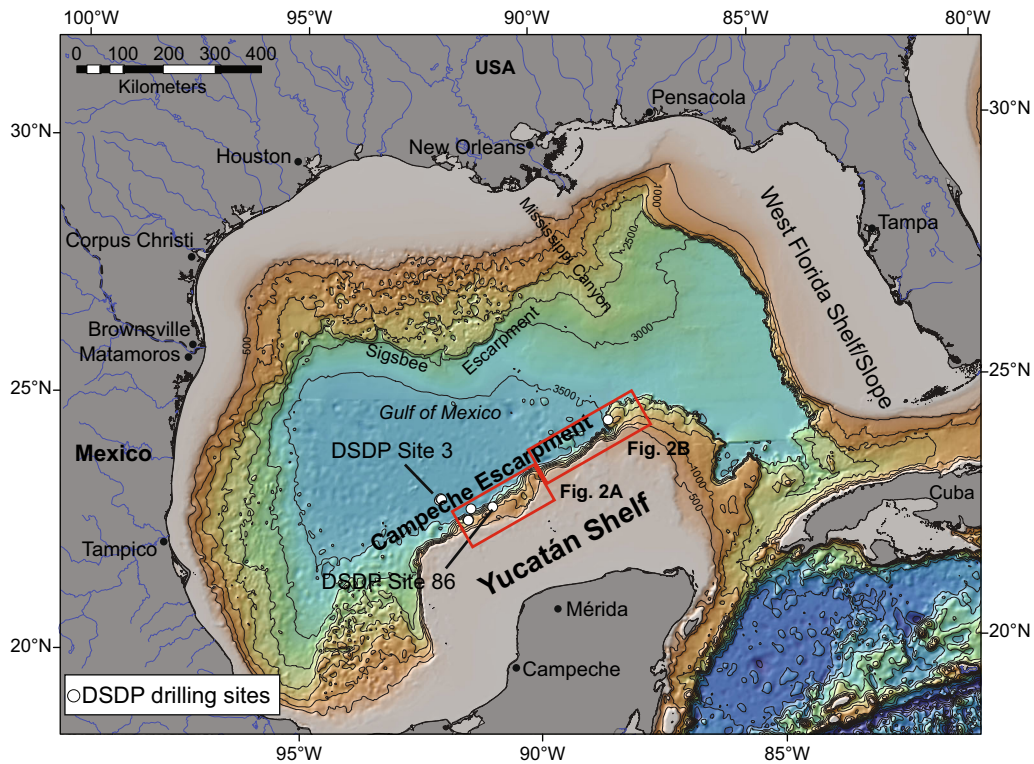


Figure 1

Bathymetry of the Gulf of Mexico (based on ETOPO1). The Yucatán Shelf/Campeche Escarpment are located along the southern margin of the Gulf, north of the Yucatán Peninsula. *Red boxes* enclose regions enlarged in Fig. 2a, b. DSDP drilling sites are indicated by the *white circles*

Yucatán Shelf edge/Campeche Escarpment and West Florida Shelf/Florida Escarpment by these early studies are now known to be due to the modification of the Yucatán Shelf through large-scale slope failure initiated by the Chicxulub impact event (Denne et al. 2013; Paull et al. 2014). Following the impact event, a thick sequence of Cenozoic age sediments, in places up more than 600 m thick, has been deposited across the Yucatán Shelf filling the failure scars along the Campeche Escarpment generated by the impact (Paull et al. 2014). Because geologically recent, large, and potentially tsunamigenic landslides that displace Cenozoic age sediments along the West Florida shelf edge have been well documented (Paull et al. 1990a, b; Chaytor et al. 2010), similar features had been thought to exist along Yucatán Shelf edge and Campeche Escarpment representing an unconstrained hazard to population and infrastructure along GOM coastlines.

In the absence of other geophysical and geological constraints, analysis of high-resolution multibeam mapping data has provided the means to estimate the dimensions of potentially tsunamigenic landslide sources along the Yucatán Shelf edge. Here we present results of source characterization analysis and regional tsunami propagation modeling for a set of prominent submarine landslide scars revealed by recently collected high-resolution bathymetric mapping data across the entire Campeche Escarpment and portions

Figure 2

a Central segment of the Yucatán Shelf/Campeche Escarpment showing the locations of four of the modeled landslide evacuation scars discussed in this study. Individual landslide scars evaluated in this study are marked in *red*, with composite scars marked in *green* (Slide 5 is a composite of Slides 1, 2 and surrounding landslide features). Shelf edge and escarpment scalloping are present throughout the segment. **b** Northern segment of the shelf and escarpment where much of shelf edge has been affected by mass wasting processes (network of landslide scarps shown in *yellow*). The location of Slides 3 and 6 are highlighted

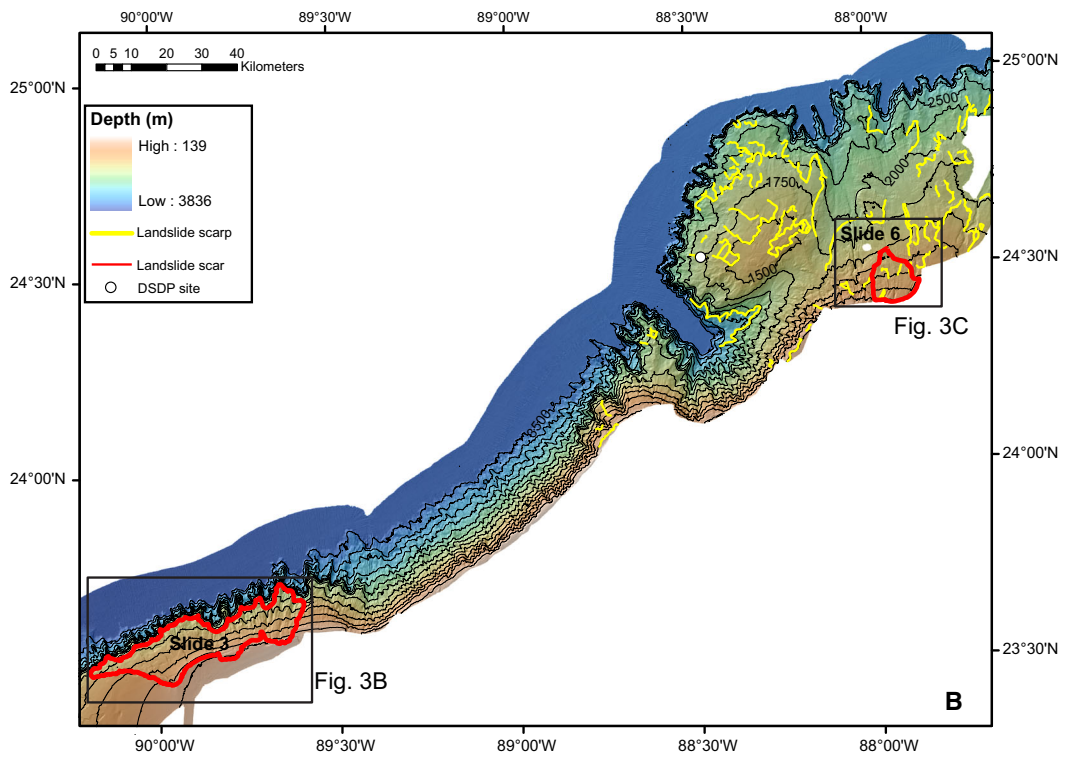
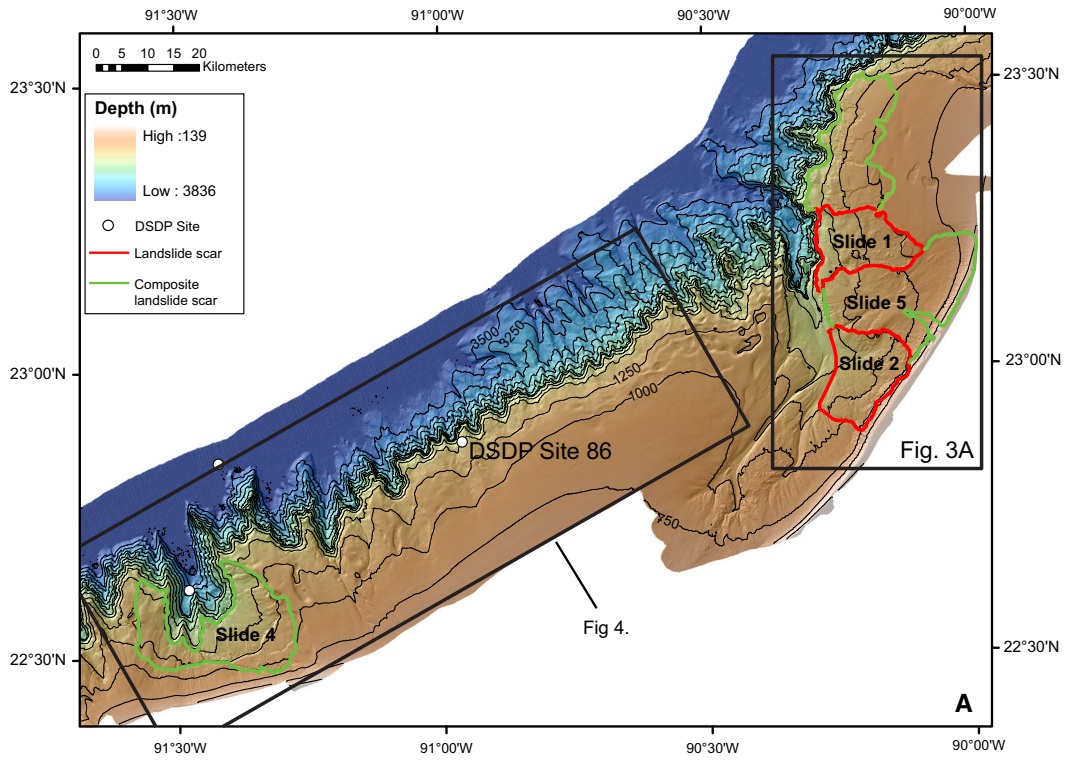


Table 1

Landslide scar (evacuation zone) dimensions calculated through GIS analysis of the bathymetric data

	Area (km ²)	GIS volume (km ³)	Modeled volume (km ³)	Max. thickness (m)	Width (km)	Length (km)	Average scarp slope (°) ^a	Max. scarp slope (°) ^a	Av. scar surface slope (°) ^b
Slide 1	198	12.5	17.0	195	11.4	17.8	25	47	3.9
Slide 2	222	36.0	31.3	390	19.5	11.5	31	52	3.3
Slide 3	578	38.0	41.1	278	63.5	11.5	32	60	6.2
Slide 4	365	21.5	20.6	253	31.0	7.7	–	–	–
Slide 5	1094	70.2	67.0	385	37.0	26.0	–	–	–
Slide 6	131	16.5	20.7	262	11.6	14.9	32	56	3.4

Modeled volumes are those calculated by COULWAVE

^a All scarps (headwall and sidewall) that bound the evacuation scar, measured at the approximate mid-point of the scarp height

^b Average of all slope values measured along a line (which is coincident with the length lines shown in Fig. 7, extending from base of the headwall scarp to the seaward end of the evacuation scar)

of the adjacent Yucatán Shelf. The primary objective of the tsunami modeling is to understand the propagation characteristics throughout the GOM, where the complex physiography of the Campeche Escarpment is thought to have a significant effect in refracting tsunami waves near the landslide sources. We also want to understand the effects that differences in the landslide parameters, such as orientation and slide dimensions, have on the relative differences in maximum amplitude throughout the GOM. Knowledge of the source parameters of landslide failures combined with basin-wide tsunami propagation characteristics are a key first step in the evaluation of regional tsunami hazards as they can inform probabilistic assessments such as recently performed by Pampell-Manis et al. (2016).

2. Data and Methods

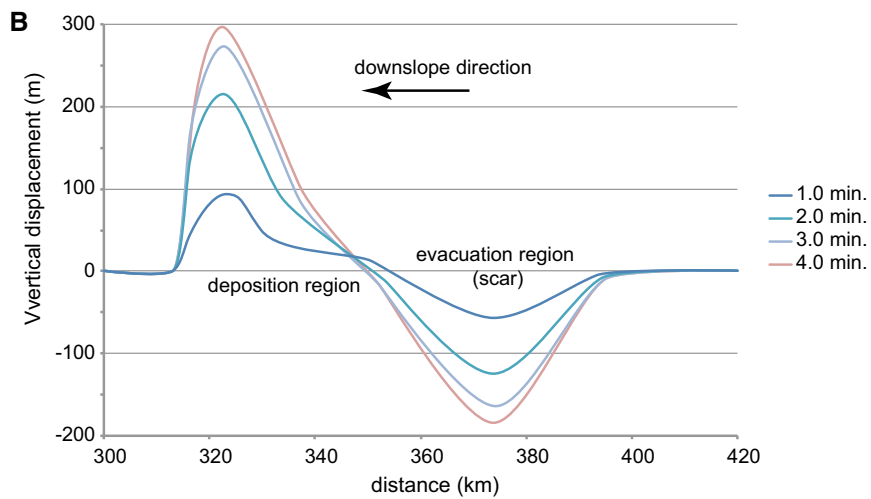
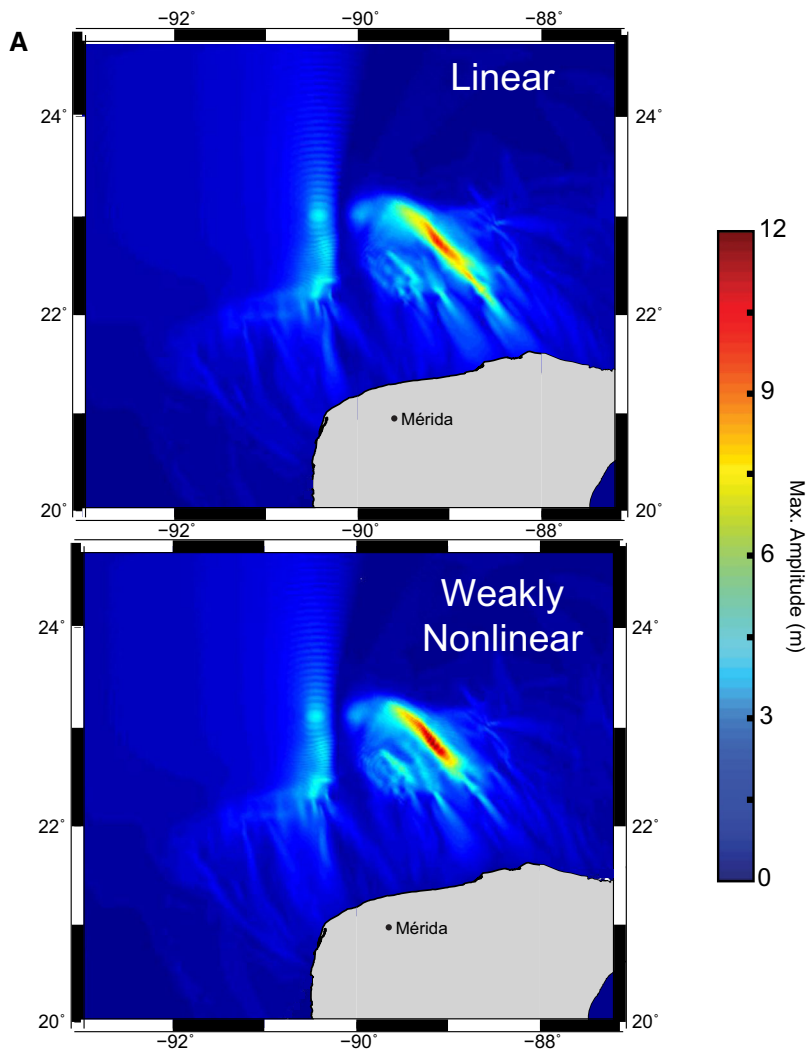
Approximately 26,500 km² of bathymetry (Fig. 2) and co-acquired acoustic backscatter data were collected along the Campeche Escarpment and Yucatán Shelf edge in 2013 using the Kongsberg EM302 multibeam echosounder installed on the *R/V Falkor* (Paull et al. 2014). These data cover the ~400–3700 m depth range along a 612 km section of the escarpment/shelf. Additional bathymetry extracted from the ETOPO1 (Amante and Eakins 2009) and NOAA Coastal Relief Model (NOAA National Geophysical Data Center, <http://www.ngdc.noaa.gov/mgg/coastal/crm.html>) were used to

Figure 3

a Comparison of maximum tsunami amplitudes (m) over 4 h for Slide 1. Using linear computations (*top*) and weakly nonlinear computations (*bottom*). **b** Time history of vertical seafloor displacement for Slide 1 used in the tsunami model. Profile oriented along slide center axis

generate the bathymetric dataset for the regional tsunami model domain. The 1 arc-minute resolution of the ETOPO1 dataset is adequate for the objectives of this study described in the previous section.

Extraction of landslide source dimensions, referred to throughout this work as landslide scars or source evacuations, including area, thickness, and volume was performed using a modification of the GIS-based analysis technique used by ten Brink et al. (2006) and Chaytor et al. (2009). The area of a failure scar is calculated as the planar area within a manually digitized bounding polygon that encompasses the region within the landslide's headwall and sidewalls. The downslope end of the scar is digitized along the top of the Campeche Escarpment or as a straight line connecting the bounding sidewalls on either flank of the landslide scar. Volumes are calculated by interpolating a smooth upper surface to the polygon that defines the boundary of each failure scar and is then subtracted from the extracted bathymetric data (lower surface). Because the sidewalls of the scar can be at a lower elevation than parts of the seafloor within the scar, the volume calculation routine assigns those high-points (negative volumes) a value of 0. As high-resolution sub-bottom profiles crossing the scars are not available, the thickness of both post-failure sediment accumulation and the material not completely



evacuated during failure are unknown and not removed from the calculated volumes. Scar length and width are measured from the digitized scar's geometric center. The average and maximum slope of the bounding headwall and sidewall scarps (Table 1) are calculated based on values extracted at ~ 50 m intervals along the approximate center of the scarps. The slope of landslide scar floors is calculated by averaging slope values extracted every 50 m along a single profile from the base of the headwall to the seaward end of the landslide scar.

Tsunami modeling was performed using the Cornell University Long and Intermediate Wave (COULWAVE) modeling package, which has been used extensively for landslide-generated tsunamis (e.g., Lynett and Liu 2002, 2005). COULWAVE solves various, depth-integrated, long-wave based equations, including the nonlinear shallow-water wave equations and weakly dispersive Boussinesq-type equations. COULWAVE has been used in similar, previous landslide tsunami studies, such as estimating tsunamis generated by the 1918 Mona Passage landslide offshore Puerto Rico (López-Venegas et al. 2008), the prehistoric Currituck landslide offshore the US Atlantic coast (Geist et al. 2009), and the 1964 Valdez landslide in Alaska (Parsons et al. 2014).

COULWAVE includes options for invoking varying degrees of nonlinearity and frequency dispersion (Lynett and Liu 2002). To broadly compare the propagation characteristics and relative distribution of maximum amplitudes throughout the GOM for each of the slide scenarios, the linearized shallow-water wave equations were first used. This modeling, however, does not accurately simulate tsunami amplitudes near the coast. For the near-field modeling, the weakly nonlinear equations were used to investigate propagation patterns from the source onto

Figure 4
a Shaded-bathymetry of Slides 1, 2 and 5 (composite slide which includes Slides 1 and 2, plus surrounding landslide scar features). Blocky debris is present in the scars of Slide 1 and Slide 2. Angular landslide scarps are prominent along the shelf/escarpment edge north of Slide 1. **b** Shaded-bathymetry of Slide 3 showing a more complicated erosional morphology of the scar floor (highlighted by the presence of a trough and ridge seaward of the bounding Slide scarp at the eastern end of the scar. **c** Shaded-bathymetry of Slide 6 at the NE end of the study region. The landslide scar truncates linear abrasion marks that are prominent on the seafloor across this section of the escarpment/shelf

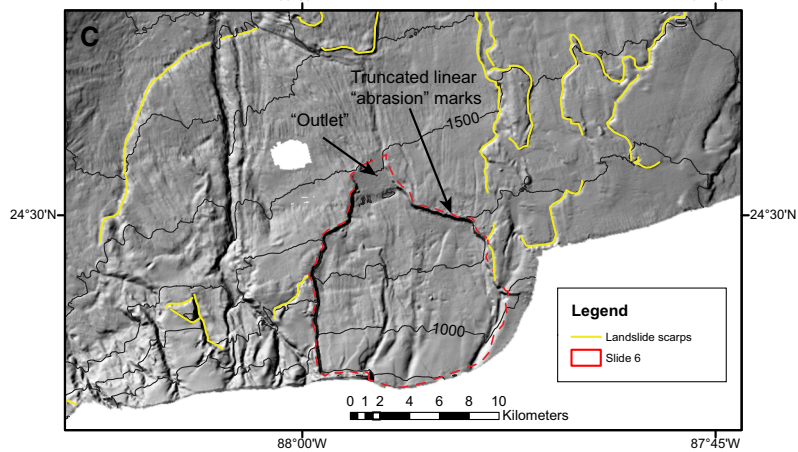
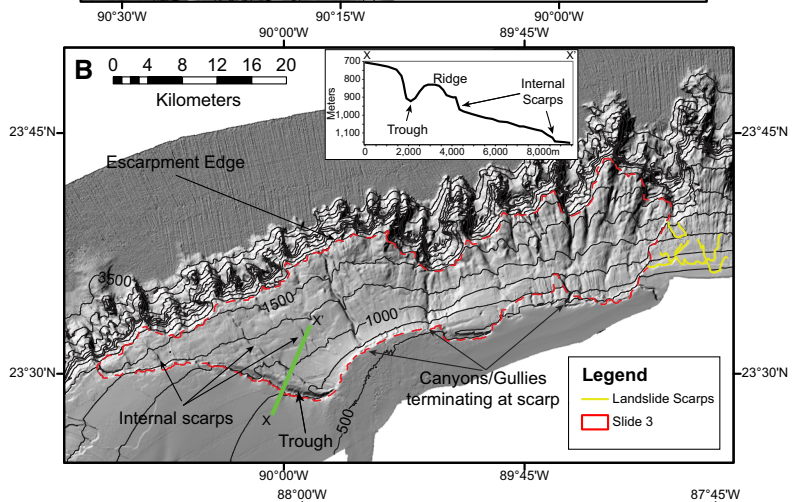
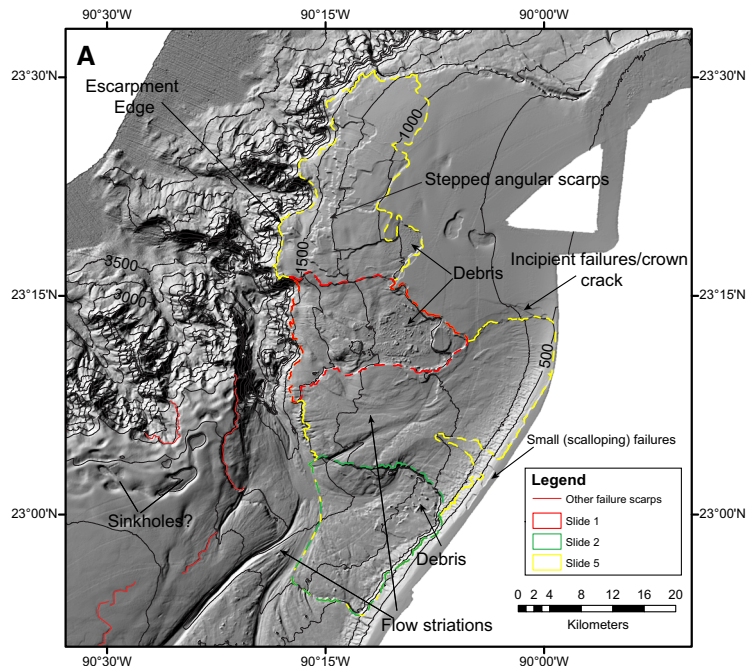
the Yucatán Shelf. The effect that the two different formulations have on tsunami amplitude for Slide 1 (Fig. 2a) is shown in Fig. 3a. Consistent with results from the Currituck landslide (Geist et al. 2009), the weakly nonlinear computation result in higher maximum amplitudes at the source, but lower maximum amplitudes near shore relative to the linear computation. For both types of simulations a Digital Elevation Model was created from the merged high-resolution multibeam bathymetry, Coastal Relief Model, and ETOPO1 regional datasets and regridded to a cell size of 1.78 km. A time step of 3.28 s was used for propagation calculations, satisfying the stability criterion for the numerical method used by COULWAVE. Sponge layer boundary conditions were used along the open-ocean boundaries. A relatively low bottom friction value (f) of 10^{-3} was used throughout the model domain, where bottom shear stress is given by $\tau = \frac{1}{2}\rho f |\mathbf{u}_b| \mathbf{u}_b$, ρ is fluid density and \mathbf{u}_b is the horizontal velocity field near the seafloor. Higher values of bottom friction would reduce the absolute amplitudes compared to those shown in the simulations. The effects of wave breaking were not included.

The source for tsunami waves is described by a geometry that approximates the mapped evacuation features of the landslides and a process time of vertical displacement in the evacuation. In terms of the spatial description of the source used in COULWAVE, the evacuation geometry is guided by lengths, depths, and widths of the mapped landslide sources given in Table 1. Deposition is assumed to occur at the base of slope and conserves the volume of the evacuation region. Smooth functions are used in COULWAVE to specify tsunami generation from landslides (Lynett and Liu 2002, 2005). The shore-normal profile involves trigonometric functions based

Table 2

Tsunami modeling parameters

Parameter	Value
Grid spacing	1.78 km
Time step	3.28 s
Bottom friction	10^{-3}
Duration	4 h



on the average slope, whereas the shore-parallel profile is based on a Gaussian function [see Lynett and Liu (2005) for specific equations]. These functions balance a realistic description of geologic processes with numerical stability required to solve the hydrodynamic equations. Smooth forcing functions for sea-surface elevations are also physically reasonable because small-scale changes in sea floor displacement are attenuated through the water column. Because the smooth functions are an approximation to the complex geometry of the mapped landslides, the volumes will be slightly different; volumes of the landslides used in the simulation are listed in Table 1 under the column “Model Volume”. Additional modeling parameters are given in Table 2.

In general, the displacement time history of the source used in COULWAVE includes both translational and rotational type motions. Because of steep bathymetric gradients associated with the Campeche escarpment, we provisionally use a primarily rotational source function to emulate foundering of the escarpment. Because there is very little horizontal translation specified for the source, there is no amplification of the tsunami due to tuning, which

occurs when the horizontal speed of the source is near the phase speed of tsunami waves (Ward 2001). The source used, therefore, is similar to tsunami generation by an earthquake, where the source is stationary and the seafloor is rotated. In contrast to an earthquake source, however, the displacements associated with landslides are larger and occur over a much longer temporal scale and a much shorter spatial scale. As an example, the time history of seafloor displacement for Slide 1 is shown in Fig. 3b. Similar to the spatial description of the source, smooth functions are used to specify the temporal history of displacement (see Lynett and Liu 2005). Peak vertical acceleration of this source is approximately 0.1 m/s^2 and occurs soon after failure. Longer source durations than what is shown in Fig. 3a would decrease the absolute tsunami amplitudes from those shown in the simulations.

To gauge the relative hazard among various landslide scenarios along the Yucatán Shelf/Campeche Escarpment using landslide dimensions indicated in Table 1, both regional modeling throughout the GOM and local modeling near the Yucatán Peninsula were conducted over 4 h of

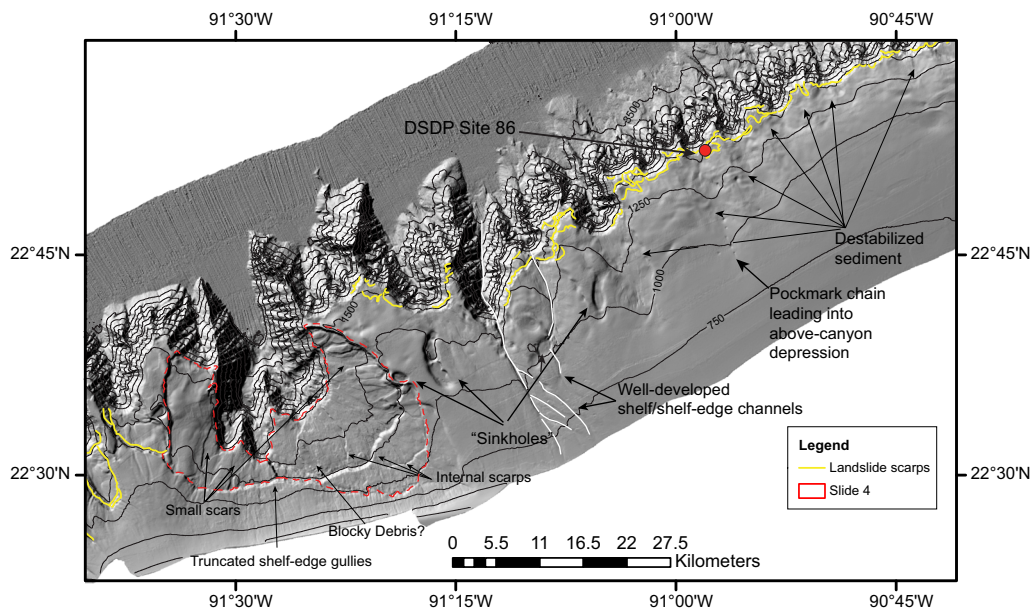


Figure 5

Central segment of the Yucatán Shelf/Campeche Escarpment showing the morphology of composite Slide 4 and its relationship to the adjacent channel cutting the escarpment. Pockmarks, sink holes and disturbed sediment, perhaps related to fluid flow and ongoing destabilization of the shelf edge occur in association with the heads of canyons cut into the shelf

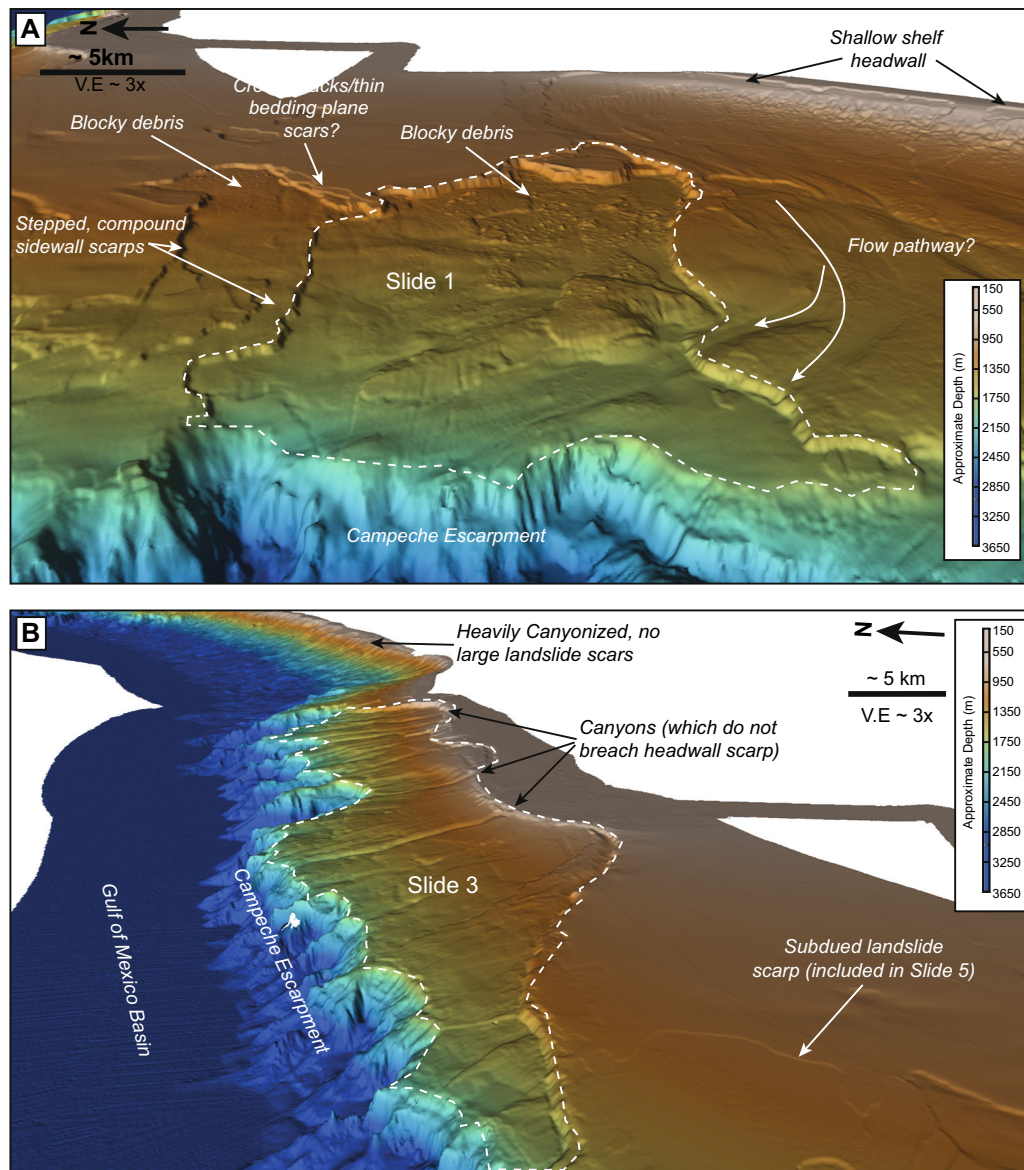
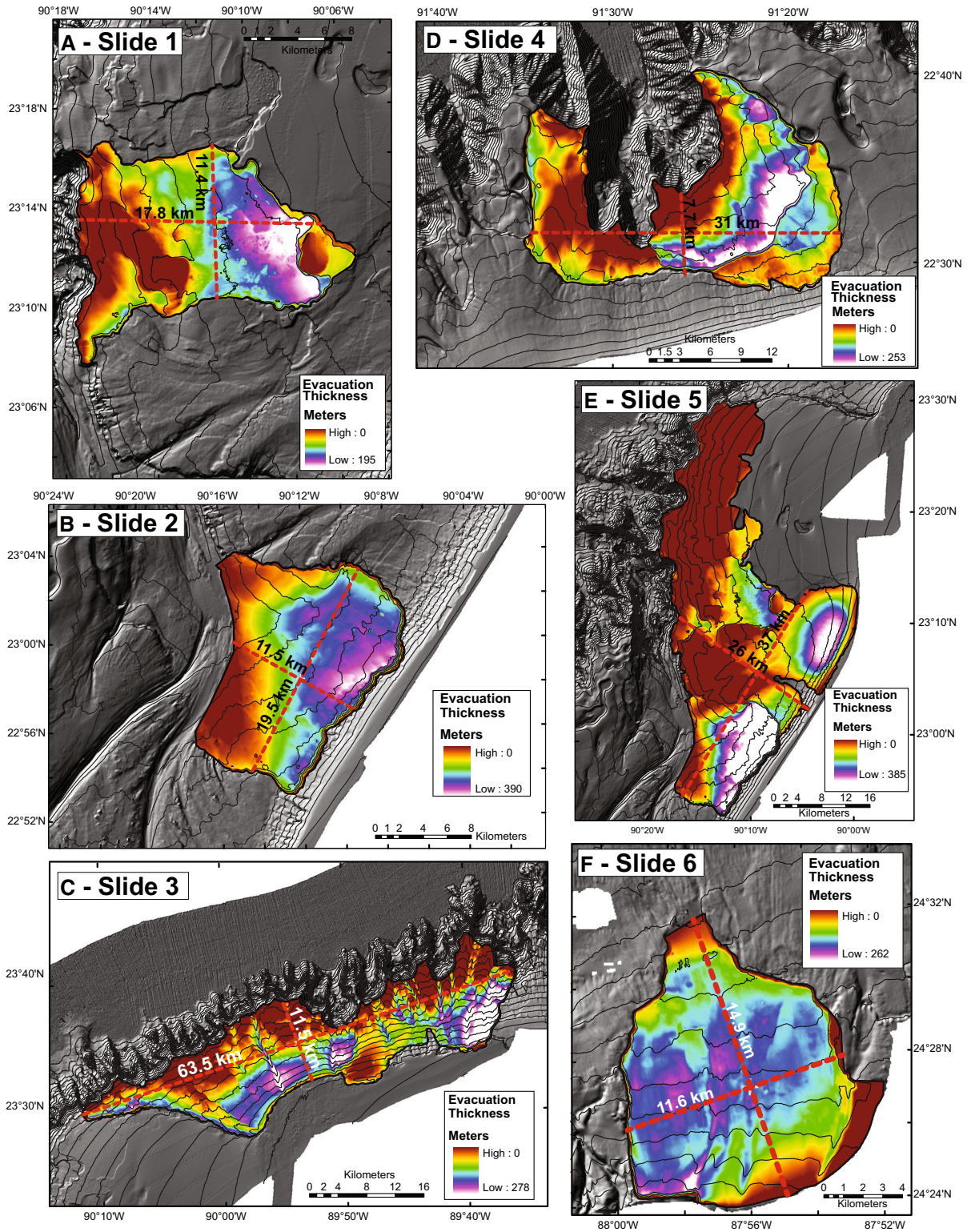


Figure 6

a Perspective view looking east across Slide 1 and adjacent landslide features comprise Slide 5. Note prominent block debris, stepped scarps and possible flow path of material that has been transported from the shallow shelf headwall area. **b** Perspective view looking NNE across Slide 3 and showing the wide and narrow nature of the scar and the canyonized nature of the eastern section of the scar. Vertical exaggeration (VE) in both images is $\sim \times 3$

propagation time. Although DSDP cores in the GOM basin north of the Campeche Escarpment (Fig. 1) contain layers composed of material most likely sourced from the Yucatán Shelf/Campeche Escarpment, burial of mass transport deposits from these landslides by younger deposits and limited availability of seismic reflection profiles, prevents

determination of deposit run-out distances. Knowledge of the deposition region, in terms of thickness and run-out distance, could provide constraints on the duration of landslide movement (e.g., Parsons et al. 2014). Landslide tsunamis in the northern GOM have also recently been modeled using a multi-phase 3-D Navier–Stokes approach that couples the dynamics of



◀Figure 7

Landslide evacuated thickness maps for each of the six landslide scars modeled. Evacuated thickness is combined with scar area to derive estimated single event landslide volumes. Maps **a–c** (Slides 1–3) and **f** (Slide 6) are assumed to represent single events, while maps **d** (Slide 4) and **e** (Slide 5) are composite events where the entire area of adjacent scars are combined into “worst case” single events

landslide movement with that of the tsunami (Horrillo et al. 2013).

3. Landslide Scar Morphology and Dimensions

Erosional scarps are wide-spread along the Yucatán Shelf and Campeche Escarpment, (Fig. 2). The largest landslide scars (Slides 1–5, Figs. 2, 3, 4, 5) appear to be primarily restricted to the central segment of the slope, removing late Cenozoic shelf sediments deposited above the Cretaceous shallow water carbonates that are exposed along the face of the escarpment. In cores recovered at DSDP Site 86 just above the upper edge of the Campeche Escarpment, these Cenozoic sediments are comprised primarily of Pleistocene-Pliocene bioturbated, clayey pelagic carbonates with some interbedded volcanic ash and Paleocene-Oligocene chalks (Worzel et al. 1970). In general, these large scars are bounded by steep, irregular-shaped headwall and sidewall scarps and by the upper edge of the escarpment, enclosing morphologically complex eroded and sediment-draped seafloor. Development of benches with shallow seaward-dipping surfaces suggests that sub-horizontal depositional surfaces may have acted as slide planes for parts of the failing mass. These sub-horizontal depositional surfaces were identified and described across the Yucatán Shelf by Lindsay et al. (1975) and Locker and Buffler (1983). The shelf edge at the northwest end of the survey area (Fig. 2a) appears to have been almost entirely modified by mass wasting processes that have removed large sections of the Cenozoic sedimentary strata. These mass wasting morphologies are almost identical to those observed along the West Florida shelf and slope (e.g., Twichell et al. 1990).

Six landslide evacuations (Slides 1–6; Fig. 2) along the central and northern shelf areas were

chosen as potential tsunami source zones (Table 1). Because the ages of the individual failures are unconstrained, two composite evacuations (Slides 4 and 5; Figs. 4a, 5) that incorporate all adjacent or nested landslide scars are characterized to provide upper bounds on the maximum failure event sizes. Slides 1, 2 and composite Slide 5 (Figs. 4a, 6a, 7a, b, e) are bounded at their seaward ends by a large debris filled unnamed canyon [area B canyon identified by Lindsay et al. (1975)]. Each of these landslide scars contain large (>100 m) detached blocks within debris that has not been fully evacuated from the scars. The floors of the remaining landslide scars are generally free of obvious debris, but the hummocky and irregular morphology of the floors of the scars suggests that they likely contain some debris and post failure pelagic/hemipelagic draping sediments. Flow-like striations between Slide 1 and Slide 2 (Figs. 4a, 6a) are similar to those visible within the unnamed canyon, suggesting that material from the shallower scar areas may have been sufficiently mobile to be transported out through the canyon. Post failure erosion of the scars and bounding scarps by downslope flows and degradation is suggested by minor channelization, small arcuate scars along the scarps, and crown-cracks in the unfailed sections adjacent to some of the main scarps (Fig. 4a). The northern end of Slide 5 (Figs. 4a, 6a) reveals a well-expressed set of stepped angular scarps that may represent exposed bedding planes.

Slide 3 (Figs. 4b, 6b, 7c) is bounded by a prominent headwall scarp that merges with the top of the Campeche Escarpment in the west and a subdued, but identifiable sidewall at its east edge that truncates small-scale landslide scarps on the adjacent shelf edge. The morphology of the eastern half of the Slide 3 scar is dominated by canyon and gully features (Figs. 6b, 7c), none of which appear to cut the headwall scarp. Internal scarps in the smoother western section of the Slide 3 scar may represent scarps resulting from additional failure events or bedding planes exposed during the one or more failure events that created the scar. An ~75–100 m deep trough (Fig. 4b) is present along a section of the headwall at the western end of the Slide 3 scar, separating the headwall from a ridge bound on its northeastern side by an internal scarp. Whether this

trough represents detachment of the ridge as part of past or incipient failure or whether it is a post failure erosional scouring along the headwall is unclear.

Slide 6 (Figs. 4c, 7f) is the only landslide scar characterized here that does not terminate at the upper edge of the Campeche Escarpment or a major canyon feature. The prominent scarps that bound the majority of Slide 6 are punctuated at its northern end by a 2–3.5 km wide, scarp bounded “outlet”. The bounding scarps of Slide 6 truncate the linear abrasion marks and widespread landslide scarps that dominate the morphology of the seafloor at the eastern most end of the bathymetry coverage of the Campeche Escarpment-Yucatán Shelf edge (Fig. 2b). The scar appears to be free of large-scale debris.

Slide 4 encompasses an arcuate zone of prominent scarps and small-scale scarps surrounding the head of a canyons system that indents into the Yucatán Shelf edge (Figs. 5, 7d). Shelf-edge gullies and other linear striations are truncated by the prominent scarp that bounds Slide 4. Linear striations are also visible extending from some of the internal scarps to the canyon rim. Except for a small area of blocky debris at the base of the bounding scarp (Fig. 4), the floor of the composite slide is largely free of visible debris.

Surficial mass transport deposits from the most recent landslides are not visible in the bathymetry at the base of the escarpment seaward of the scarps, but Pliocene to early Pleistocene-age carbonate debris and turbidites, possibly sourced from Yucatán Shelf landslides, were encountered in DSDP Site 3 (Ewing et al. 1969) ~50 km north of the Campeche Escarpment (Fig. 1). Large slump blocks have been identified at the base of the escarpment (Locker and Buffler 1983; Paull et al. 2014) but the age of their emplacement is unknown.

Along the shelf edge northwest of Slide 4 (Fig. 5), depressed seafloor, pockmark trails, and subtle channelization are visible within the sediment cover and are aligned with most of the canyon heads. Small failure scarps where these depressed and deformed sediments merge with the heads of the canyons suggest that these areas may be in the early stages of retrogressive failure, perhaps driven by subsurface fluid migration. A similar distribution of surficial pockmark and instability features have been described for portions of the Olbia continental slope,

offshore Sardinia (Dalle Valle and Gamberi 2011) where they occur within the buried paleochannels leading to the canyon heads and adjacent to the Capbreton and Zaire canyons where sediment disorganization is thought to be due to upward movement of pore water and fault pathways (Mulder 2011). Seismic reflection profiles across these canyon and pockmark features will be required evaluate the processes responsible for their formation.

4. Tsunami Modeling Results and Discussion

Comparison of the maximum amplitude distributions from tsunami simulations of the six mapped landslide scenarios (Fig. 8) reveals some important differences. The largest tsunamis are associated with the landslide scarps with the largest width (Slide 3) and highest volume (Slide 5). Overall, the basin-wide severity of the tsunami is approximately proportional to the volume of the evacuated region. Aside from the volume, landslide width has the most effect on far-field tsunami amplitudes for cases studied here, although the moderate width of Slide 5 leads to higher tsunami amplitudes because of the greater maximum thickness and hence, greater volume. Ideally, tsunami amplitude is greatest along an azimuth coincident with the direction of slide movement, such as exhibited by Slide 6 (Fig. 8f). For the other slides, however, complex physiography along the Campeche Escarpment refracts tsunami waves in the immediate vicinity of the source toward a wide range of azimuths. For example, Slides 1, 2, and 5 have a more westerly direction of landslide movement resulting in increased relative amplitudes along the Mexican Gulf Coast, but substantial tsunami energy also arrives at the US Gulf Coast locations. Because of its extensive width, Slide 3 is the most effective at focusing tsunami energy south to the Yucatán Peninsula and north to the US Gulf Coast.

For each scenario (Figs. 8), the largest tsunami amplitudes are at the source, decreasing as the tsunami propagates in deep water. As the tsunami approaches the continental shelf, the amplitude increases owing to shoaling amplification. Tsunami amplitude generally peaks at the shelf edge and gradually diminishes toward shore, owing to attenuation from bottom

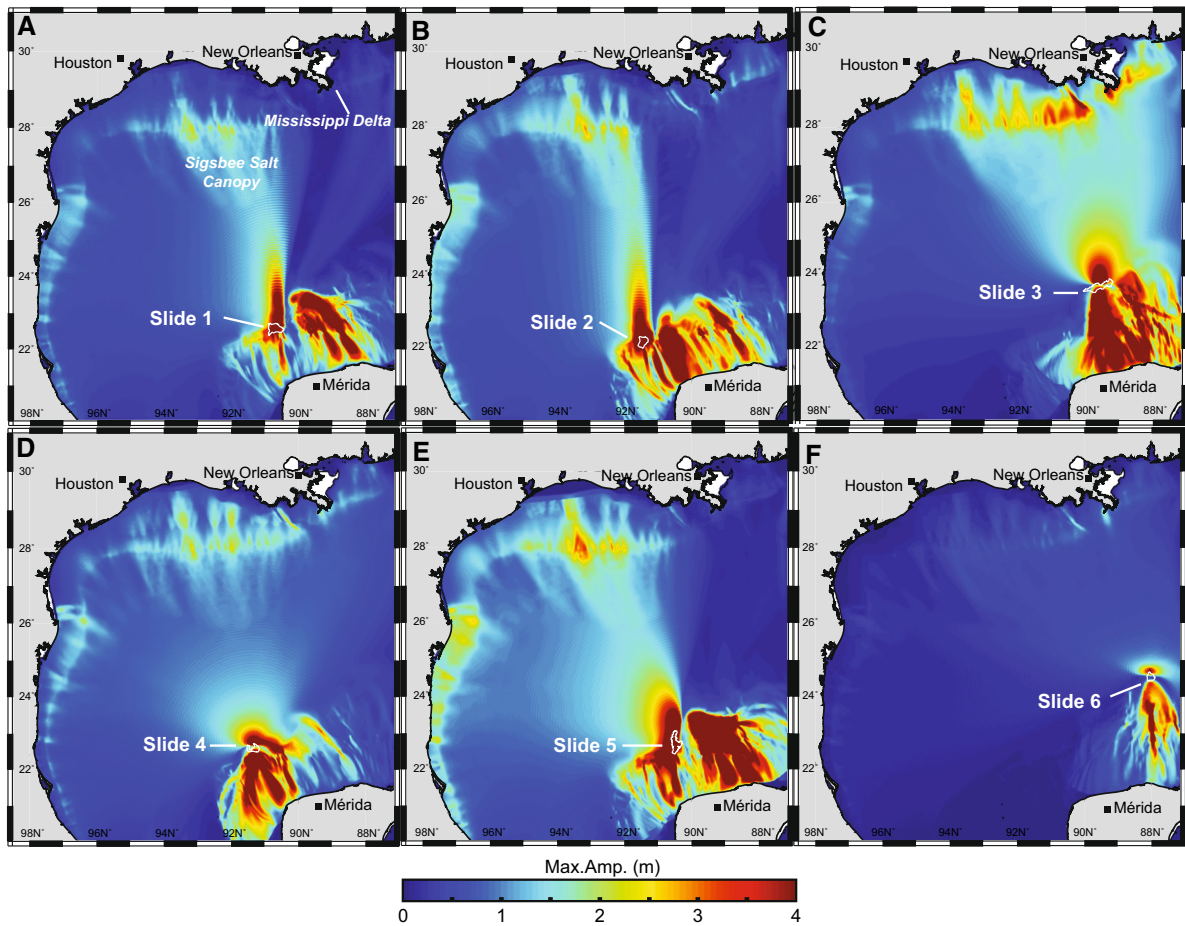


Figure 8

Maximum tsunami amplitude maps (4 h of propagation) for modeled landslide sources, Slides 1–6 (a–f). Approximate boundaries of the source landslide scars shown by white polygons

friction. As the tsunami propagates to the northern GOM from the south, large-scale bathymetric features such as the Sigsbee Escarpment/salt canopy and Mississippi Canyon/Delta (Figs. 1, 8) focus amplitudes toward the east Texas and Louisiana coastline (Fig. 8). For the southward propagating tsunami, because of the short propagation distance, tsunami amplitudes are highest for each scenario along the northern Yucatán Peninsula coastline (Figs. 8). In general, wider shelves lessen the severity of tsunami runup at the coast compared to runup at coastal locations adjacent to narrower shelves. The nearshore maximum amplitudes at these far-field locations would be slightly less if the weakly nonlinear wave equations were used (Fig. 3a).

In the near-field, there are complex refraction effects associated with the landslide tsunamis as shown by example for Slide 3 (Fig. 9). Tsunami waves propagating toward the Yucatán Peninsula have a leading trough phase, originating from the evacuation region. In addition, however, the positive amplitude phase from the deposition region is refracted by the continental slope, resulting in a leading peak phase to the east of the leading trough phase (30 min). At 45 min, the trailing peak phase of the western set of waves starts to overrun the leading trough phase, as amplitudes gradually dissipate across the shelf. Refraction of the tsunami emanating from the deposition region towards the shoreline was also observed for the other landslide scenarios, except

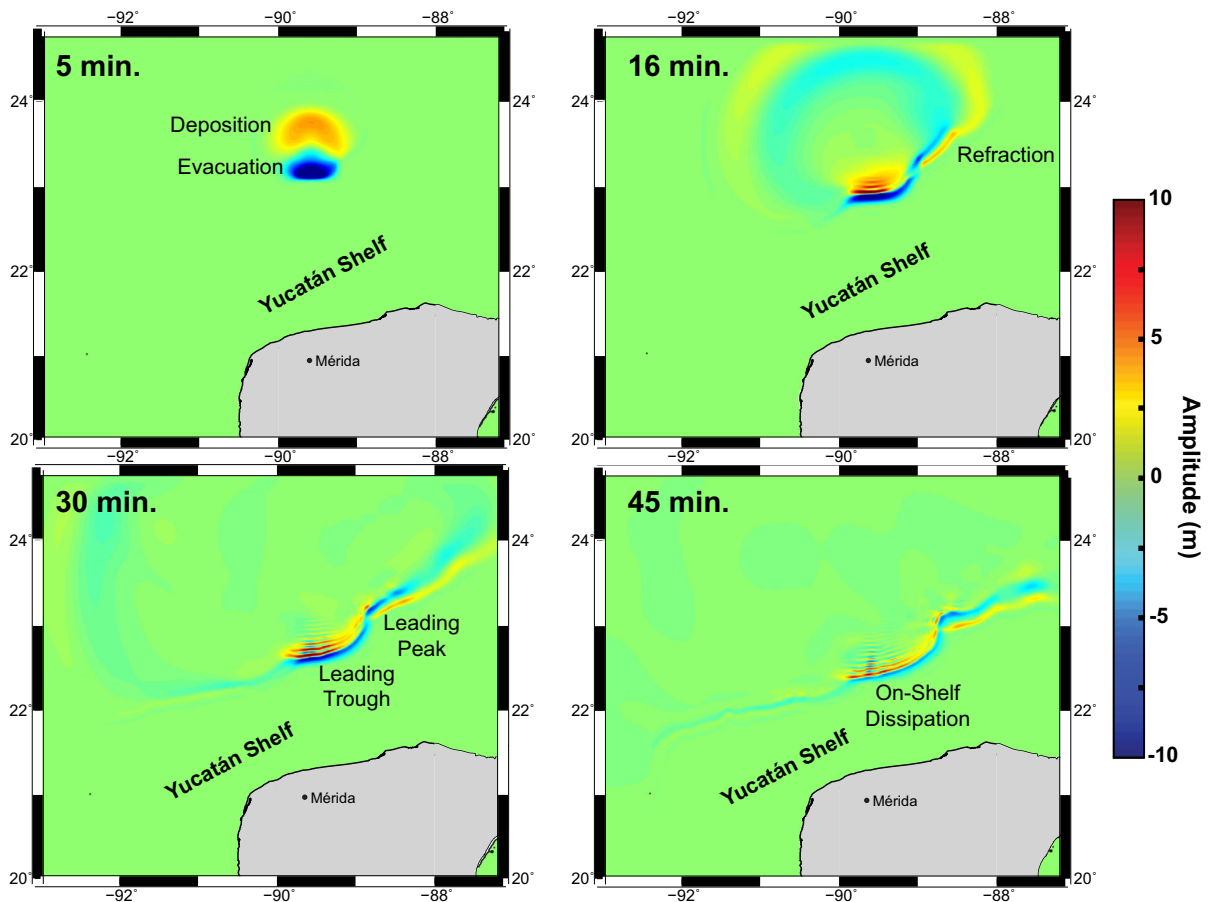


Figure 9

Time snapshots of the near-field refraction pattern of waves generated by Slide 3 (Fig. 4c) showing overrun of the leading trough phase from the evacuation by the leading positive phase from the refracted wave as amplitudes gradually dissipate across the shelf

for Slide 6. This refraction phenomenon results in a greater length of shoreline in the near-field affected by the tsunami than would be expected from simple shoreward propagation of the tsunami from the evacuation region. A similar refraction processes was also observed in the simulation of a hypothesized tsunami from the Currituck Landslide, offshore the eastern US (Geist et al. 2009) and may be common for tsunamis generated by continental slope landslides.

Detailed determination of tsunami inundation on land requires much finer resolution of bathymetry and topography in the shelf and near-shore regions than is used in this study or available throughout the GOM. Even more important, tsunami severity is critically dependent on the time history of landslide movement

and that is currently unconstrained for the Yucatán Shelf/Campeche Escarpment landslides.

5. Conclusions

High-resolution mapping data reveals that the Yucatán Shelf/Campeche Escarpment margin has been intensely modified by Cenozoic mass wasting processes along almost its entire length. While landslides originating along Yucatán Shelf/Campeche Escarpment or any other GOM region have not been directly linked to known or inferred Cenozoic tsunami events, the presence of large landslides throughout the GOM Basin highlights the need for further detailed deterministic and probabilistic hazard

analysis. In the absence of other geophysical and geological constraints, analysis of high-resolution multibeam mapping data has provided the means to estimate the dimensions of potentially tsunamigenic landslide sources along the Yucatán Shelf edge. Modeling these sources, at least to a first approximation, shows that they would have been capable of generating tsunamis that could propagate throughout the GOM Basin. Relative differences in maximum amplitude and propagation characteristics relate primarily to slide orientation and dimension, although the physiography of the Campeche Escarpment has a complex effect on wave propagation near each source (except for Slide 6). Bottom friction effects on the shelf likely would reduce impact of generated tsunamis along the US Gulf Coast, but the proximity of the Yucatán Peninsula to the sources may lead to large wave amplitudes along the Peninsula's northern coast. Although tsunami waves may have limited amplitudes along the US Gulf Coast, widespread flood-prone coastal zones throughout the GOM and enhanced strong currents propagating through channel and river networks (Horrillo et al. 2010) could lead to flooding and damage across some coastal communities. Additional constraints on landslide sizes, failure conditions, and the mobility of the failed masses, development of landslide chronologies along the Yucatán Shelf and adjacent areas, assessment of future landslide locations and higher resolution tsunami modeling will be vitally important to better understanding potential future hazards.

Acknowledgments

We would like to acknowledge the assistance of the Schmidt Ocean Institute, the captain and crew of the R/V *Falkor*, the David and Lucile Packard Foundation, Eve Lundsten, Krystle Anderson, and Brian Andrews. Nathan Miller, Uri ten Brink, David Tappin, and three anonymous reviewers provided helpful reviews which improved the manuscript. Any use of trade, product, or firm names is for descriptive purposes only and does not imply endorsement by the US Government.

REFERENCES

- Adatte, T., Stinnesbeck, W., & Keller, G. (1996). Lithostratigraphic and mineralogic correlations of near K/T boundary clastic sediments in northeastern Mexico: Implications for origin and nature of deposition. In G. Ryder, D. Fastovsky, S. Gartner (Eds.), *The Cretaceous–Tertiary event and other catastrophes in earth history: Boulder, Colorado*, Geological Society of America Special Paper 307, 211–226.
- Amante, C., & Eakins, B.W. (2009). *ETOPO1 1 arc-minute global relief model: Procedures, data sources and analysis*. NOAA Technical Memorandum NESDIS NGDC-24. National Geophysical Data Center, NOAA. doi:[10.7289/V5C8276M](https://doi.org/10.7289/V5C8276M).
- Bourgeois, J. T., Hansen, A., Wiberg, P. L., & Kauffman, E. G. (1988). A tsunami deposit at the Cretaceous–Tertiary boundary in Texas. *Science*, 241, 567–570.
- Bryant, W. R., Meyerhoff, A. A., Brown, N. K., Furrer, M., Pyle, T., & Antoine, J. W. (1969). Escarpments reef trends, and diapiric structures, eastern Gulf of Mexico. *Bulletin American Association of Petroleum Geologists*, 53, 2506–2542.
- Chaytor, J. D., ten Brink, U. S., Solow, A. R., & Andrews, B. D. (2009). Size distribution of submarine landslides along the US Atlantic margin. *Marine Geology*, 264(1–2), 16–27.
- Chaytor, J.D., Twichell, D.C., Lynett, P., & Geist, E.L. (2010). Distribution and tsunamigenic potential of submarine landslides in the Gulf of Mexico. In: D.C. Mosher, L. Moscardelli, R.C. Shipp, J.D. Chaytor, C.D. Baxter, H.J. Lee, & R. Urgeles (Eds.), *Submarine mass movements and their consequences, advances in natural and technological hazards research (745–754)*, vol 28. Springer, Netherlands.
- Dalle Valle, G., & Gamberi, F. (2011). Pockmarks and seafloor instability in the Olbia continental slope (northeastern Sardinian margin, Tyrrhenian Sea). *Marine Geophysical Researches*, 32, 193–205.
- Denne, R. A., Scott, E. D., Eickhoff, D. P., Kaiser, J. S., Hill, R. J., & Spaw, J. M. (2013). Massive Cretaceous–Paleogene boundary deposit, deep-water Gulf of Mexico: New evidence for widespread Chicxulub-induced slope failure. *Geology*, 41, 983–986.
- Ewing, M., Worzel, J. L., Beall, A. O., et al. (1969). *Initial reports of the deep sea drilling project* (Vol. 1). Washington D.C.: U.S. Government Printing Office.
- Geist, E. L., Lynett, P. J., & Chaytor, J. D. (2009). Hydrodynamic modeling of tsunamis from the Currituck landslide. *Marine Geology*, 264, 41–52.
- Horrillo, J., Wood, A., Kim, G. B., & Parambath, A. (2013). A simplified 3-D Navier Stokes numerical model for landslide-tsunami: Application to the Gulf of Mexico. *Journal Geophysical Research*, 118, 6934–6950.
- Horrillo, J.J., Wood, A.L., Williams, C., Parambath, A., & Kim, G.-B. (2010). Construction of tsunami inundation maps in the Gulf of Mexico, Tech. Rep, National Tsunami Hazard Mitigation Program (NTHMP), National Weather Service Program Office, NOAA.
- Lawton, T. F., Shipley, K. W., Aschoff, J. L., Giles, K. A., & Vega, F. J. (2005). Basinward transport of Chicxulub ejecta by tsunami-induced backflow, La Popa basin, northeastern Mexico, and its implications for distribution of impact-related deposits flanking the Gulf of Mexico. *Geology*, 33, 81–84.

- Lindsay, J. F., Shipley, T. H., & Worzel, J. L. (1975). Role of canyons in the growth of the Campeche Escarpment. *Geology*, *3*, 533–536.
- Locker, S. D., & Buffler, R. T. (1983). Comparison of lower Cretaceous carbonate shelf margins, northern Campeche Escarpment and northern Florida Escarpment, Gulf of Mexico. *American Association of Petroleum Geologists. Studies in Geology*, *15*, 123–128.
- López-Venegas A.M., ten Brink U.S., Geist E.L (2008). Submarine landslide as the source for the October 11, 1918 Mona Passage tsunami: Observations and modeling. *Marine Geology*, *254*(1), 35–46.
- Lynett, P., & Liu, P. L. F. (2002). A numerical study of submarine landslide generated waves and runup. *Proceedings of the Royal Society of London, Ser. A*, *458*, 2885–2910.
- Lynett, P., & Liu, P. L. F. (2005). A numerical study of the run-up generated by three-dimensional landslides. *Journal of Geophysical Research: Oceans*, *110*, C03006. doi:10.1029/2004JC002443.
- Mulder, T. (2011). Gravity processes and deposits on continental slope, rise and abyssal plains. In H. Huneke & T. Mulder (Eds.), *Deep-sea sediments* (pp. 25–125). Amsterdam: Elsevier.
- National Geophysical Data Center/World Data Service (NGDC/WDS): Global Historical Tsunami Database. National Geophysical Data Center, NOAA. doi:10.7289/V5PN93H7.
- Pampell-Manis, A., Horrillo, J., Shigihara, Y., & Parambath, L. (2016). Probabilistic assessment of landslide tsunami hazard for the northern Gulf of Mexico. *Journal of Geophysical Research Oceans*. doi:10.1002/2015JC011261.
- Parsons, T., Geist, E. L., Ryan, H. F., Lee, H. J., Haeussler, P. J., Lynett, P., et al. (2014). Source and progression of a submarine landslide and tsunami: The 1964 Great Alaska earthquake at Valdez. *Journal Geophysical Research*. doi:10.1002/2014JB011514.
- Paull, C. K., Caress, D. W., Gwiazda, R., Urrutia-Fucugauchi, J., Rebolledo-Vieyra, M., Lundsten, E., et al. (2014). Cretaceous–Paleogene boundary exposed: Campeche Escarpment, Gulf of Mexico. *Marine Geology*, *357*, 392–400.
- Paull, C. K., Freeman-Lynde, R., Bralower, T. J., Gardemal, J. M., Neumann, A. C., D'Argenio, B., et al. (1990a). Geology of the strata exposed on the Florida Escarpment. *Marine Geology*, *91*, 177–194.
- Paull, C. K., Spiess, F. N., Curray, J. R., & Twichell, D. (1990b). Origin of Florida Canyon and the role of spring sapping on the formation of submarine box canyons. *Geological Society of America Bulletin*, *102*, 502–515.
- Shaw, C. E., & Benson, L. (2015). Possible tsunami deposits on the Caribbean coast of the Yucatán Peninsula. *Journal of Coastal Research*, *31*, 1306–1316.
- ten Brink, U. S., Geist, E. L., & Andrews, B. D. (2006). Size distribution of submarine landslides and its implication to tsunami hazard in Puerto Rico. *Geophysical Research Letters*, *33*, L11307.
- Twichell, D. C., Parson, L. M., & Paull, C. K. (1990). Variations in the styles of erosion along the Florida Escarpment, eastern Gulf of Mexico. *Marine and Petroleum Geology*, *7*, 253–266.
- Ward, S. N. (2001). Landslide tsunami. *Journal of Geophysical Research: Solid Earth*, *106*(B6), 11201–11215.
- Worzel, J.L., Bryant, W., Beall Jr., A.O., Capo, R., Dickinson, K., Foreman, H.P., Laury, R., McNeely, B.W., & Smith, L. (1970). Site 86 Initial Reports of the Deep Sea Drilling Project 10, Texas A & M University, Ocean Drilling Program, College Station, TX, United States, pp 25–47.

(Received January 27, 2016, revised May 16, 2016, accepted June 21, 2016, Published online August 8, 2016)